Acta Materialia 195 (2020) 468–481

Contents lists available at ScienceDirect

Acta Materialia

journal homepage: www.elsevier.com/locate/actamat

Full length article

Toughening magnesium with gradient twin meshes

Xin Wang[a], Lin Jiang[a], Chase Cooper[a], Kehang Yu[a], Dalong Zhang[a], Timothy J. Rupert[a], Subhash Mahajan[b], Irene J. Beyerlein[c], Enrique J. Lavernia[a], Julie M. Schoenung[a,*]

[a] Department of Materials Science and Engineering, University of California-Irvine, CA, USA
[b] Department of Materials Science and Engineering, University of California-Davis, CA, USA
[c] Mechanical Engineering Department, Materials Department, University of California-Santa Barbara, CA, USA

ARTICLE INFO

Article History:
Received 1 December 2019
Revised 7 May 2020
Accepted 9 May 2020
Available online 17 May 2020

Keywords:
Magnesium
Strengthening
Deformation twinning
Gradient structure
Micropillar compression

ABSTRACT

In the present study, we combine comprehensive site-specific microstructural and mechanical characterization studies to evaluate the toughening effect induced by applying a surface SPEX milling (SSM) approach to commercially-pure Mg. Our results show that the high frequency, multi-directional deformation strain induced by SSM generated gradients in the grain size and orientation with depth from the surface. More importantly, it also resulted in a gradient in the density of twin meshes, which are defined as two or more intersecting arrays of twins, along the sample thickness direction. Tensile tests at room temperature indicate that after SSM, the samples have higher ultimate tensile strengths and two-fold increases in ductility as compared to those of the untreated samples. The effect of the initial texture and SSM parameters on the microstructural evolution and texture randomization were analyzed by electron backscattered diffraction (EBSD). Furthermore, in order to correlate the variation in microstructure with the site-specific mechanical response, TEM and *in-situ* micropillar compression testing in SEM were performed at various distances from the SSM-treated surface. The results show that twin meshes may be responsible for the activation of more slip systems and higher strain hardening, which result in higher uniform plastic strain.

1. Introduction

Hexagonal close packed (HCP) metals usually exhibit poor ductility in comparison to that of cubic structured metals due to their low symmetry crystal structure [1-3]. Large differences in the activation stresses among the predominant slip and twinning systems are characteristic of HCP metals. In Mg, basal slip, which deforms the crystal along the ⟨a⟩ axis, is the most readily activated deformation mode, while the slip modes that deform the crystal in the ⟨c⟩ axis are much more difficult [4, 5]. The critical resolved shear stress (CRSS) value reported for basal slip is less than 1 MPa, while that for prismatic slip is approximately 40-50 MPa in pure Mg [5]. Deformation twinning, frequently observed in the {10-12}<10-1-1> system, also plays a role to accommodate non-basal strain to a certain extent [2, 6]. Much effort has recently been devoted to enhancing concurrently the strength and ductility of Mg, enabling it to be employed as a lightweight engineering structural metal in many more applications in the automotive and aerospace industries than in use today. However, Mg, like most metals, is challenged by the strength/ductility paradox, in which methods to enhance strength leads to reductions in ductility and vice versa.

It has been reported that twin boundaries (TBs) in face center cubic (FCC) metals, such as copper [7-11] and austenitic steels [12-14], have the potential to circumvent this paradox providing strengthening, without losing ductility. This result is explained to originate from dislocation accumulation at and interactions with TBs [7-10]. TBs can obstruct the motion of dislocations, like regular grain boundaries, although less effectively. Yet, some dislocations in FCC metals can glide along and transfer across TBs via dislocation-TB interactions, which is beneficial to material deformation. As supported by early studies back in the 1970s [15, 16], in nanostructured FCC metals, twins can accommodate stress concentrations associated with slip bands and twin-twin intersections by activating dislocation slip inside or on the exit side of twins. The twin-slip and twin-twin interactions of HCP metals, however, are much more complicated than those in the FCC metals, since there are many more distinct modes of slip and twinning, with vastly differing characteristics [1, 6]. Moreover, unlike in FCC metals, deformation twinning has been widely reported in coarse-grained pure Mg and Mg alloys at room temperature [2], and not often observed in nanostructured Mg and Mg alloys [17]. Twin propagation and intersections are often associated with twin chains, slip bands and stress concentrations and could be responsible for instabilities or loss of ductility [18, 19]. However in one recent study [20] using an Mg-4%Li alloy, fine networks of intersecting twins and double twins, or twin meshes, developed in the grains during deformation, and it was reported that the twin-mesh configuration did not lead to

* Corresponding author.
E-mail address: julie.schoenung@uci.edu (J.M. Schoenung).

https://doi.org/10.1016/j.actamat.2020.05.021
1359-6454/

premature failure or weakening, compared to the same alloy with finer grains and no twins. Therefore, it is a scientifically interesting question whether twin mesh can promote strengthening and plasticity in HCP metals.

Deformation twins generated by monotonic straining and their effect on the subsequent deformation response have been explored in Mg alloys. For instance, {10-12} twins induced by pre-compression have demonstrated a positive effect on the material properties during recompression in hot-rolled AZ31 [21, 22]. However, in Mg after uniaxial pre-compression, only a single twin variant forms in a majority of grains because the highly texture material placing most of the grains in an orientation favorable for twinning. Due to the predominance of one twin variant, increases in compressive strength and ductility after pre-straining is limited [21, 22]. Moreover, although twins are profuse in Mg after uniaxial deformation, the easy propagation and growth of the common {10-12} twin type adds technical challenges to the development of a stable, high twin density, and fine twin mesh structure. Successful approaches to harden twin boundary motion in Mg, include segregation of alloying elements at twin boundaries [23], formation of lamellar-shaped precipitates [24, 25] and, most cost-effectively, via formation of twin-twin intersections [26]. As such, it is hypothesized that deformation methods that generate multiple types and/or variants of twins at the grain level could promote finer twin meshes and an enhanced combination of strength-ductility in Mg.

Surface mechanical attrition treatment is a newly developed deformation approach to create a gradient structure with severe grain refinement at the material surface, resulting in multi-directional and localized plastic deformation at the sample surface [27-32]. Several recent studies have demonstrated that the application of this approach to HCP Ti [33] and Mg alloys [34-36] can activate a high density of twins and twin meshes embedded in a gradient structure. Distinct from dislocation-dominated grain refinement processes in FCC metals, twins and twin meshes in HCP metals play an important role in the grain refinement and texture evolution in the different sample layers. However, due to a gradient structure, the effect of twins on the mechanical response of Mg remains poorly understood, and requires careful spatial microstructural characterization and mechanical testing.

In the present study, we use SPEX milling, which is conventionally used for pulverizing and mixing powders, to generate repetitive and multi-directional impacts onto a sample surface to create twin meshes within grains of polycrystalline pure Mg. Different surface SPEX milling (SSM) parameters (i.e., ball size and impact velocity) were employed to investigate their influence on the microstructure developed. Using a suite of microscopy techniques, ranging from optical microscopy to electron backscatter diffraction (EBSD) and transmission electron microscopy (TEM), the microstructures created as a function of depth from the SSM-treated Mg were closely examined. We show that this method can create a gradient microstructure with twin meshes comprised of different types and variants of twins. Most significantly, we demonstrate that the material containing twin meshes not only strengthens the material but also increases its ductility two-fold compared to coarse-grained Mg.

2. Experimental Methods

The starting material in this study is an as-rolled commercially pure Mg sheet (99.9%, Goodfellow Corporation, Oakdale, PA) 6 mm in thickness. Tables 1 lists the chemical composition of the starting material as specified by the supplier. The as-received Mg sheet was annealed in a tube furnace at 200 °C for 2 hours to minimize dislocations and twins prior to the surface treatment.

2.1. Surface SPEX milling (SSM) treatment

SSM treatment was carried out in air at room temperature using a SPEX 8000 M Mixer/Mill equipped with a cylindrical stainless-steel grinding vial. Mg foil samples ~ 12 × 6 × 1 mm were sectioned using electrical discharge machining (EDM) with two different orientations, 1) perpendicular and 2) parallel to the normal direction (ND) of the rolled Mg sheet. These two samples are hereby designated as perpendicular-type and parallel-type samples, respectively. The samples were polished with SiC grinding paper down to grade 1200 and then attached to the end plate of the grinding vial using a carbon adhesive tape. Spherical steel balls with clean and smooth surfaces were loaded in the vial as milling media. To generate samples with appropriate microstructural gradients for our investigation into twin formation and mechanical response, nine samples were treated with selected sample orientations, steel ball sizes, and milling times. Table 2 presents the designations for these samples. Both sides of the foils were milled for 2 min with an operating clamp speed of 1080 cycles/min. The impact velocity in the SSM process is approximately 2 m/s. To achieve a more uniform distribution of ball impacts on the sample surface, the SSM treatment was interrupted every 30 s, in order to rotate the grinding vial by 90°.

Table 1
Chemical composition (wt. %) of the as-received commercially pure Mg sheet.

Al	Cu	Fe	Mn	Ni	Si	Zn	Mg
0.007	0.002	0.028	0.017	<0.001	0.005	<0.002	Balance

2.2. Microstructural characterization

The SSM-treated samples were sectioned along the cross-sectional (CS) plane and mechanically polished and etched with a 20% HCl ethanol solution. This treatment prepared these etched CS surfaces for imaging using an optical microscope (OM, Axio A.1, Carl Zeiss, Germany). To optimize the surface condition of the samples for EBSD microstructural analysis, the CS sample surfaces were ion-polished by a cross-section polisher (Model SM-09010, JEOL). EBSD analysis was performed in a scanning electron microscope (SEM, FEI Quanta 3D) equipped with an HKL EBSD detector. The voltage and beam current used for EBSD data collection were 30 kV and 12 nA, respectively. The step size for EBSD data collection was 1 μm. Post-processing of the EBSD data was carried out using Channel 5 system from HKL Technology. Samples for site-specific TEM at different depths beneath the treated surface were prepared by standard focused ion beam (FIB) lift-out method on a polished CS sample surface. A low ion beam current of 10 pA was used for final surface cleaning to minimize the damage layer induced by FIB. The TEM microstructural analysis was performed using a JEOL 2100F operated at 200 kV.

2.3. Mechanical testing

The effect of selected SSM treatment conditions on the mechanical properties of Mg was studied by uniaxial tensile tests and SEM *in-situ* compression of cylindrical micropillars. To perform tensile tests, dog-

Table 2
Surface SPEX milling (SSM) treatment parameters.

Specimen number	Operating clamp speed (Hz)	Diameter of steel balls (mm)	Orientation of the treated surface relative to the normal direction	Treatment time on each side (min)
M1	17.67	0.1	Parallel	2
M2	17.67	0.3	Parallel	2
M3	17.67	0.9	Parallel	2
M4	17.67	2	Parallel	1
M5	17.67	2	Perpendicular	1
M6	17.67	2	Parallel	2
M7	17.67	2	Perpendicular	2
M8	17.67	6.4	Parallel	5
M9	17.67	12.7	Parallel	0.5

bone shaped samples with a gage length of 4 mm and 1 × 1 mm cross section were cut from the SSM-treated Mg foils using EDM. For comparison, tensile samples with the same geometry were also sectioned from as-annealed Mg without SSM treatment. Tensile tests were conducted using an Instron E3000 testing system at room temperature with a constant nominal strain rate of 10^{-3} s^{-1}. The deformation strain was measured by a non-contacting video extensometer. For each condition, two repeated samples were tested with the tensile direction parallel to the rolling direction. The tests were carried out to failure and in every case, fracture occurred within the gage section.

In-situ compression was carried out using a PI-85 Picoindentor system (Bruker/Hysitron Inc.) equipped with a flat-top conical diamond probe 20 μm in diameter inside an FEI Quanta 3D SEM. Mg micropillars with diameters ~5 μm and a height-to-diameter aspect ratio of ~3:1 were machined by FIB over the sample cross sectional area at various distances (~80, ~180, ~280 and ~370 μm) away from one SSM-treated surface. Similar for all FIB sample preparation processes, a low ion beam current of tens of pA was used as a final step to clean the micropillar surfaces in order to minimize the FIB damage. After the final cleaning procedure, the taper angle for all the micropillars was less than 2° SEM *in-situ* compression was performed under displacement-controlled testing mode with an indentation rate of 15 nm/s (i.e., a nominal strain rate of 10^{-3} s^{-1}) and a maximum indentation depth of 3 μm. *In-situ* movies were recorded during compression in the SEM.

3. Results

3.1. Microstructure of the SSM-treated Mg samples

The impacts from the balls at the surface are expected to cause a gradient in strain rate and accumulated strain from being high at the surface and diminishing with depth. OM was used to analyze the resulting gradient in microstructure. In Fig. 1, we present representative CS microstructures from the SSM-treated sample, sample M6 in this case, as observed by OM. The micrographs illustrate the formation of a gradient structure from the surface to the center of the foil. Profuse twin lamellae formed, and a higher density exists closer to the SSM-treated surfaces. Moreover, grain refinement was observed in the regions next to the SSM-treated surfaces with the very top layers showing grain sizes below the resolution of OM.

From the OM analysis, we have identified three distinct microstructural regions in the SSM-treated Mg samples based on proximity from the treated surface: I. a nanocrystalline or ultrafine grained layer; II. a refined structure region, in which the sizes of grains are smaller than that in the as-received samples; III. a deformed coarse grain region, with grain sizes on the order of the initial grain size, containing profuse deformation twin lamellae.

The microstructures of the as-annealed and SSM-treated samples were further investigated using EBSD, the results of which are shown in Fig. 4. In these figures, the grains are color-coded relative to the horizontal direction, which is the surface normal direction for the SSM-treated samples. Before SSM treatment, the microstructure consists of nearly equiaxed grains, with an average grain size of ~80 μm, which are almost free of deformation twins. Hot rolling produced a strong basal texture characterized by the single peak observed in the (0002) pole figure, indicating that the c-axis of a majority of the grains were aligned about the normal direction (ND). The peak texture intensity in the units of multiples of uniform density (m.u.d.) is indicated in each pole figure.

The SSM-induced microstructures (Fig. 2 (b-j)) vary with the treatment parameters. The SSM-treated surface is on the right side of each map. When small balls (0.1 mm in diameter) were used, lamellar-shaped deformation twins were not extensive after SSM treatment. With an increase in the size of steel balls or treatment time, a deformed layer, containing profuse lamella-shaped deformation twins, formed close to the treated surface and grew thicker. The frequency of finding intersecting twin-twin junctions in grain interiors also increased as the density of the deformation twins increased. Together with an increment in twin density, the occurrence of low angle grain boundaries, as indicated by the gray lines in the EBSD maps, also increased. Also, micron to submicron-sized fine grains formed close to the SSM-treated surface, as shown in Fig. 2 (d - f), provided that the ball size and time are sufficiently large and long, respectively. The top layer regions could not be indexed and appear dark in the EBSD maps, a likely result of the high residual strain and small grain sizes. Yet it is clear that the fraction of fine grains increases with the increase in steel ball size and treatment time. As the bulk deformation behavior of Mg largely depends on the crystallographic texture, sample orientation is also expected to impact the SSM-treated microstructures. Two perpendicular-type samples, M5 and M7, were examined in this study. In comparison to the lamellar shaped twins in parallel-type samples, twins in the perpendicular-type samples seen in Fig. 2 (f) and (h) are more irregular in shape. In addition, more contraction twin boundaries, which are colored in light blue, were found in perpendicular-type samples. The strong basal texture in the initial material was randomized after SSM treatment. Multiple peaks appear in the basal pole figures of the SSM-treated samples, as seen in the insets of Fig. 2 (c-j), indicating the <c>-axes were tilted away from the normal direction of the Mg foil.

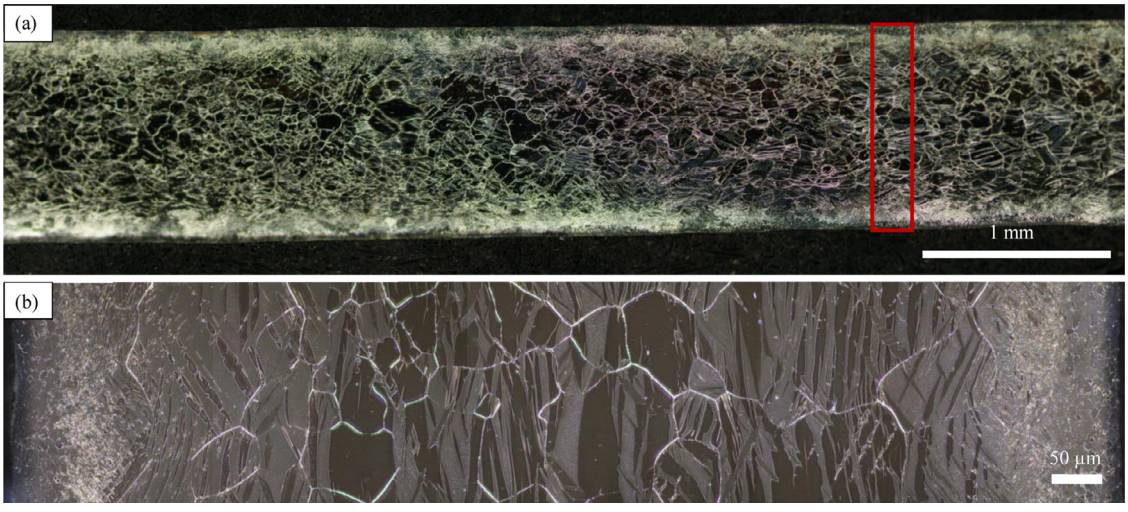

Fig. 1. (a) Optical micrographs of the cross sections of SSM treated sample M6. (b) is the magnified image of the area in (a) marked by the red rectangle.

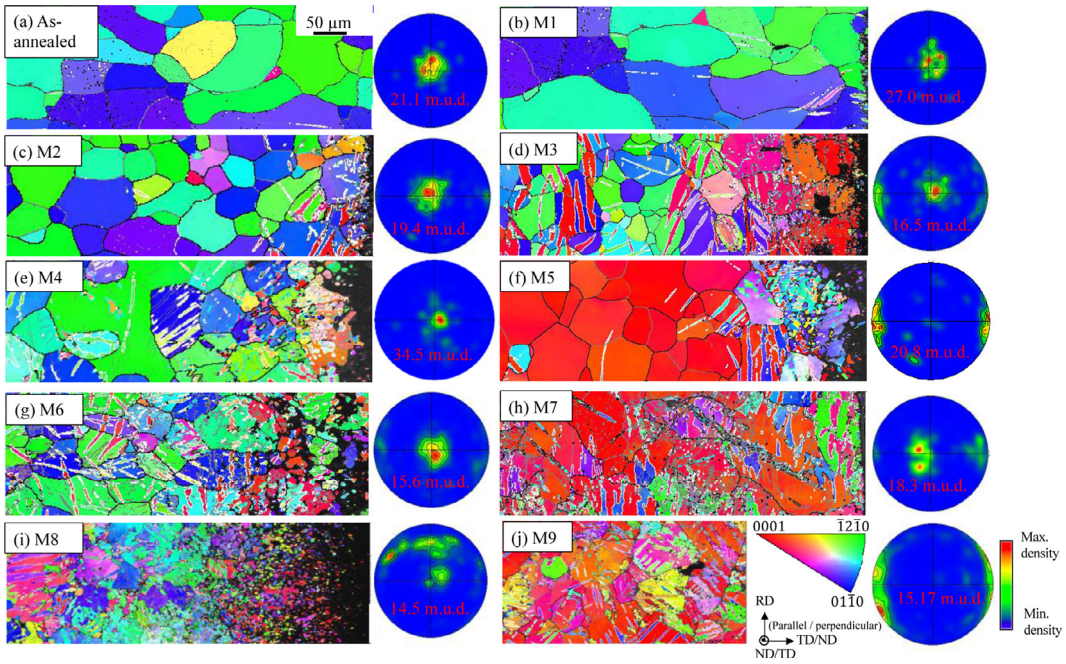

Fig. 2. EBSD inverse pole figure (IPF) colored maps of the cross-sectional surface of the SSM treated Mg foils and the corresponding {0001} pole figures: (a) As-annealed sample, (b) M1, (c) M2, (d) M3, (e) M4, (f) M5, (g) M6, (h) M7, (i) M8, (j) M9.

3.2. TEM observations at various distances beneath the SSM-treated sample surface

Further effort has been devoted to reveal the twin mesh development and grain refinement process during SSM treatment. Due to the gradient variation in strain and strain rate along the sample thickness, the microstructural evolution under different levels of strain and strain rates can be examined by TEM at different depths beneath the SSM-treated surface. Specimens at depths of ~200, 100, and 50 μm from the surface for sample M7 were prepared for TEM investigation.

3.2.1. ~200 μm below the SSM-treated surface

In the deformed layer ~200 μm below the SSM-treated sample surface, TEM reveals profusely twinned grains containing twin lamellae with thicknesses varying from hundreds of nanometers to several microns (Fig. 3 (a-c)). The bright and dark field TEM images in Fig. 3 (a, b) show parallel twins within a grain. The diffraction spot from the twin domain was selected to form the dark field image in Fig. 3 (b). Some intersecting twins were also observed at this depth, as seen in Fig. 3 (c). In addition, a high density of dislocations can be observed in both the matrix regions and within the twin lamellae (Fig. 3 (a-c)), including dislocation pile-ups near the grain boundaries (Fig. 3 (d)).

3.2.2. ~100 μm below the SSM-treated surface

Compared to the ~200 μm layer, more grains with intersecting twins were observed in the layer ~100 beneath the treated surface. A transmission Kikuchi diffraction (TKD) map taken at a representative intersecting twin lamellae structure, as shown in Fig. 4 (a), contains two different {10-12} extension twin variants, T5 and T6, both of which have ~86° misorientation relationship with the matrix but with a different ⟨11-20⟩ zone axis. The crystallographic orientations for the twin lamellae and matrix are indicated by the superimposed HCP unit cells in the TKD map. The mapped area also illustrates that twin boundaries developed in the SSM-treated sample are not straight, which suggests that these twin boundaries contain copious incoherent segments and defects as a result of local stresses induced by the ball impacts. The TEM bright field image of the same sample region is shown in Fig. 4 (b). The selected area electron diffraction (SAED) pattern (inset in Fig. 4 (b)), acquired from the area delineated by the red circle when the T6 twin boundary is nearly “edge on”, confirms that the T6 variant is a {10-12} extension twin. Low angle grain boundaries visible in Fig. 4 (b), as marked by a yellow box, correspond to dislocation walls seen in Fig. 4 (c) with higher magnification. Furthermore, the bright field image at the twin-twin junction in Fig. 4 (d) reveals that the contrast in the twin-twin intersecting region within T6 is different from that for the rest of T6, indicating a small misorientation angle between them. These low angle misorientation boundaries in the vicinity of the twin-twin intersection regions indicate the presence of complex strain localization.

3.2.3. ~50 μm below the SSM-treated surface

TEM examination of the layer ~50 μm below the SSM-treated surface of sample M7 reveals evidence of microstructural refinement. The bright and dark field images in Fig. 5 (a, b) show the formation of submicron spaced lamellae bands, as marked by the yellow arrows. A high density of dislocations is observed on and near the lamellae boundaries. The twin lamellae that are observed further below at depths of ~200 and ~100 μm are not observed at ~50 μm. Instead, the microstructure at ~50 μm is comprised of micron to submicron polygonal grains. As seen in Fig. 5 (c, d), the refined polygonal grains are irregular in shape, having grain sizes in the range of 500-1500 nm. Some fragmented twin lamellae are also visible in this region. It is plausible that these twin fragments are remnants of twins after slip-twin reactions that were subsequently subdivided by the formation of subgrains during the SSM treatment. Evidence of accumulated strain in this region appears as variations in the contrast within the twin lamellae and Mg matrix due to lattice deformation. The lattice deformation suggests that subdivision of matrix grains and twin lamellae into polygonal blocks joined by subgrain boundaries leads to further grain refinement. In some regions, the deformed microstructure is characterized by more uniformly distributed ultrafine grains, as shown in Fig. 6. From the TEM bright and dark field

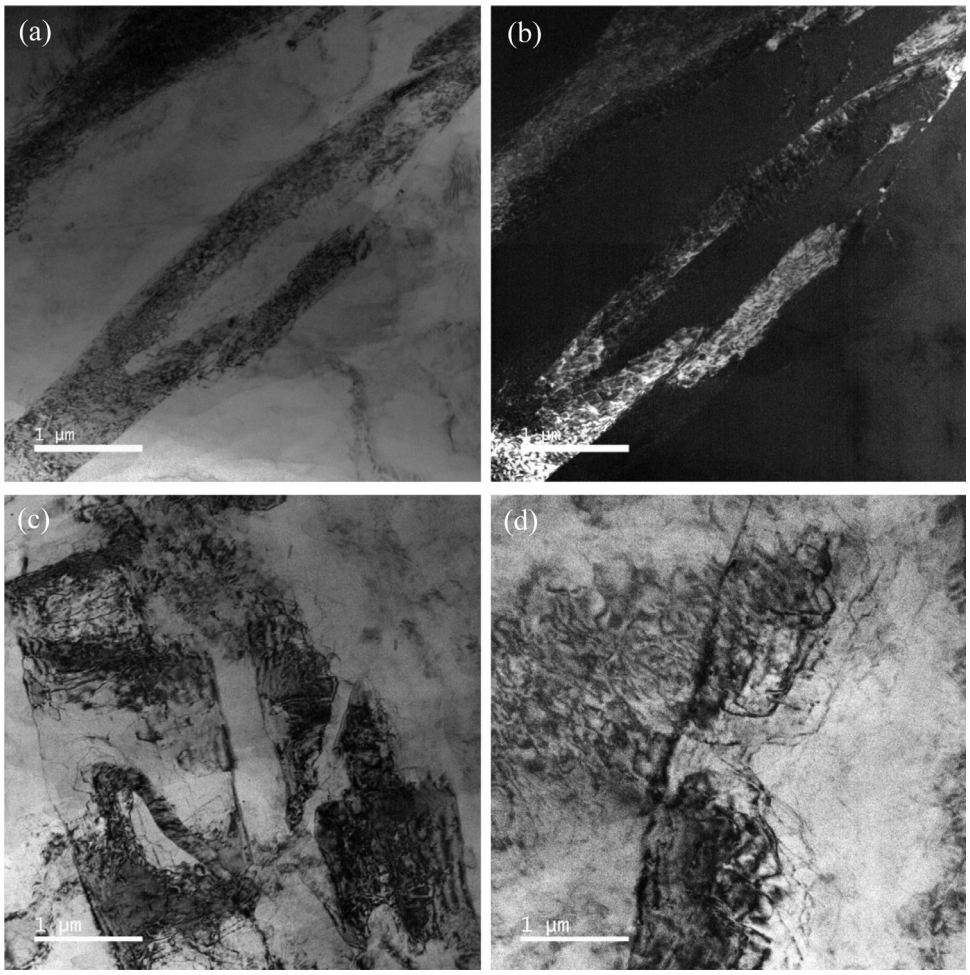

Fig. 3. Microstructure of sample M7 at 200 μm below the SSM-treated surface: (a) Bright field and (b) dark field TEM images of twin lamellae; (c) A bright field image of intersecting twin lamellae and high density of dislocations; (d) Dislocation pile up adjacent to a grain boundary.

images, it can be determined that the uniformly distributed ultrafine grains have an average grain size of ~500 nm.

3.3. Mechanical properties and deformed microstructure

3.3.1. Tensile tests

Uniaxial tensile tests were carried out at a strain rate of 10^{-3} s^{-1} at room temperature. The tensile direction was parallel to the rolling direction of the Mg sheet, which triggers non-basal slip in rolled Mg with a strong basal texture. In addition to an untreated rolled Mg sample, selected SSM-treated samples, M6 and M7, with the same geometry, were also tested to examine the effect of the SSM treatment on mechanical properties. The stress-strain curves are shown in Fig. 7, and the corresponding tensile property data are summarized in Table 3. The ultimate tensile strength (UTS) mildly increases from 207 MPa (as-annealed) to 223 MPa (sample M6) and 230 MPa (sample M7) after SSM treatment, while the tensile ductility increases by more than a factor of two. The as-annealed Mg sample shows a rapidly decreasing strain hardening rate and failed at a limited true strain of 2.9%. In comparison, the strain hardening rates in samples M6 and M7 decrease less rapidly after yielding, consistent with the more uniform elongation seen in these two samples than in the as-annealed one. The 0.2% offset yield strength $\sigma_{0.2\%}$ decreases by 34% and 4% for samples M6 and M7, respectively, after SSM treatment, which can be related to the weakening of the initial rolling texture.

Sample M7, after tensile deformation, was further characterized using EBSD. Fig. 8 (a, b) displays the EBSD IPF-colored map and kernel average misorientation (KAM) map, respectively. Compared to the microstructure of sample M7 prior to the tensile test (the IPF-colored map in Fig. 2 (h)), twins that are irregular in morphology and lower in density are observed in the sample after tension, which is likely a result of slip-twin interactions and plastic relaxation due to detwinning. The KAM map is used to indicate the locally stored strain energy and density of geometrically necessary dislocations. In general, KAM values are slightly higher adjacent to the SSM-treated surface. Some high KAM values are found at grain boundaries, triple junctions or extending from the grain boundaries to the grain interior. Additionally, there are high KAM values at locations inside the grains, with many of them close to the remaining twin boundaries. The storage of dislocations at both grain boundaries and grain interiors, such as at deformation twin boundaries, may be responsible for the enhanced strength of this SSM-treated sample.

3.3.2. In-situ *compression in the SEM*

The enhanced simultaneous tensile ductility and UTS displayed by SSM-Mg foils in tensile testing can be attributed to the special SSM-induced microstructure. These foils, however, are comprised of a heterogeneous structure, described by visible changes in grain size, orientation, and twin-mesh density with depth from the surface. *In-situ* compression of micropillars fabricated at select distances from the SSM-treated surface provides a way to examine the variation in mechanical behavior along the thickness from the treated surface. A series of micropillars were fabricated along the CS surface of sample M7 at: (A) ~80 μm, (B) ~180 μm, (C) ~280 μm and (D) ~370 μm

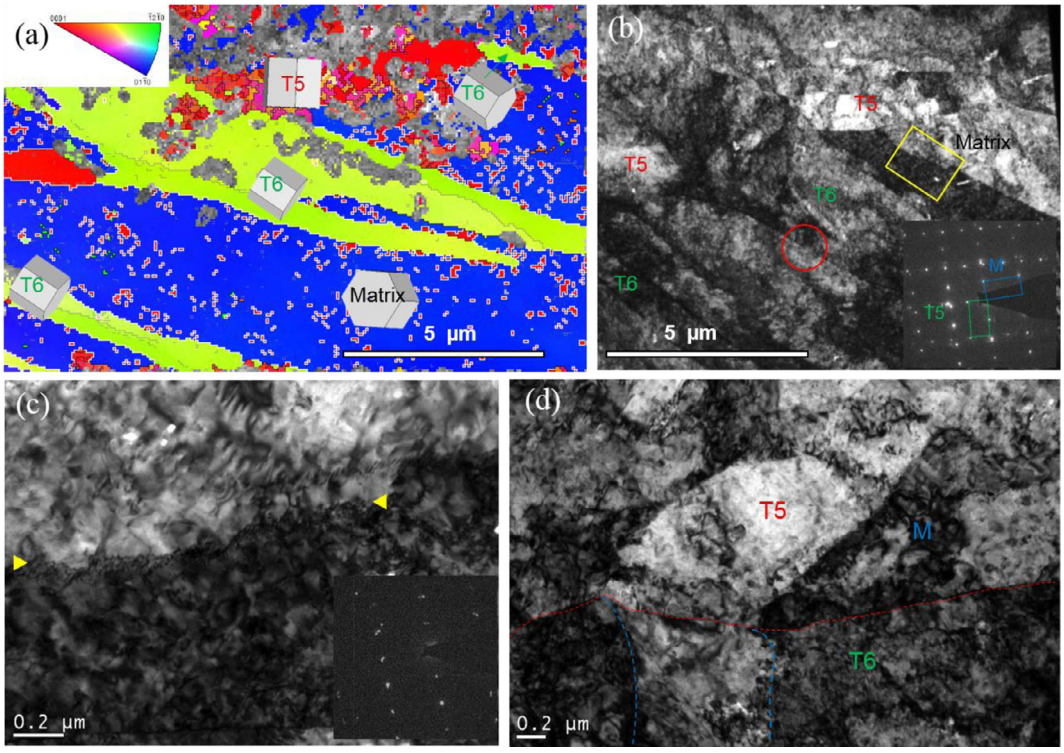

Fig. 4. Microstructure of sample M7 at 100 μm below the SSM-treated surface: (a) Transmission Kikuchi diffraction map of a twin-twin joint region. T5 and T6 denote the two different twin variants. The HCP unit cells indicate the crystallographic orientations for the twin lamellae and matrix; (b) TEM bright field image of the same region in (a). Inset is the selected area electron diffraction pattern acquired from the twin boundary area marked by the red circle. (c) A higher magnification image of the dislocation wall structure visible in the yellow box in (b) and the corresponding diffraction pattern. The yellow arrows mark the position of the dislocation wall; (d) A higher magnification image at the twin-twin boundary.

from the SSM-treated surface. The compression direction for all micropillars was parallel to the rolling direction of sample M7, which will favor {10-12} extension twins during compression in matrix grains with initial basal texture. Within the twinned domains, the compression axis is along pyramidal planes considering the twin-induced lattice reorientation. Therefore, basal slip can easily activate within the twins and twin meshes due to the relatively high Schmid factor and extremely low CRSS.

Engineering stress-strain curves obtained by compression of the four series of micropillars are shown in Fig. 9. For all four samples, sigmoidal shaped stress-strain curves were obtained, which is characteristic of deformation dominated by the formation of {10-12} extension twins in bulk samples [37]. The yield strength $\sigma_{0.2\%}$ for micropillar A is the highest (~70 MPa) relative to micropillars B (~57 MPa), C (~58 MPa) and D (~51 MPa). In addition to having the highest yield stress, micropillar A also exhibited the highest strain hardening rate after yield among the four micropillars. The stress-strain curve for micropillar A (Fig. 9 (a)) shows discrete non-catastrophic intermittent stress drops after the stress-plateau regime at high stress levels. These stress drops are non-catastrophic as the stress does not decrease to close to zero before it starts to strengthen again. In contrast, for the samples further away from the SSM-treated surface, stress drops were observed within the stress-plateau regime at lower stress and strain values, as shown in Fig. 9 (b, c), corresponding to catastrophic shear events, as seen in the corresponding recorded videos (see Supplementary Videos S1-S4 for the SEM compression of micropillars A-D, respectively).

The failure modes for the micropillars can be observed, as shown in the SEM images taken after *in-situ* compression, see Fig. 10. Micropillars C and D failed by gliding of the top part relative to the bottom part of the micropillars along a parallel set of slip planes. Micropillar B shows a similar deformed micropillar shape as micropillars C and D, but the gliding steps seen on the sample surface are along two intersecting sets of planes. Micropillar A, however, shows a distinct deformed micropillar shape compared to micropillars B to D. The micropillar expands laterally during compression. Moreover, the surface of micropillar A is slightly kinked and multiple shallow gliding steps in different orientations are visible, but none of the steps cut through the whole micropillar to cause catastrophic failure.

4. Discussion

4.1. Microstructural evolution during SSM treatment

The highly anisotropic slip systems in HCP Mg make non-basal slip on the prismatic and pyramidal planes relatively difficult to activate [38, 39], which hinders achieving a sufficient number of independent slip systems to satisfy the von Mises criterion [40]. Therefore, besides dislocation slip, deformation twinning plays an important role in the deformation of Mg at room temperature. Multiple twinning modes have been observed in Mg, including the extension twins {10-12}<-1011> and {11-21}<-1-126> and contraction twins {10-11}<10-1-2> and {11-22}<11-2-3> [16]. Among all of them, the {10-12} extension twin, which is favored under <c>-axis extension, has received the most attention in the scientific literature, as it is the easiest twinning mode in Mg [6], due to the relatively small twinning shear. The other commonly observed type of twin in Mg is the {10-11} contraction twin, which forms under <c>-axis compression. Distinct from {10-12} twins that can thicken to consume the entire grain, {10-11} twins are usually scarce and narrow in the Mg lattice [41, 42], and can nucleate a second {10-12} twin inside their domain [20, 43].

The microstructural investigation in this study (Figs. 2 and 3) revealed dislocations and {10-12} extension twins in the region close to the center of the Mg foil, which experienced low strains and strain rates, indicating these deformation modes were activated in the very early stage of SSM treatment. Compared to uniaxial deformation modes, the

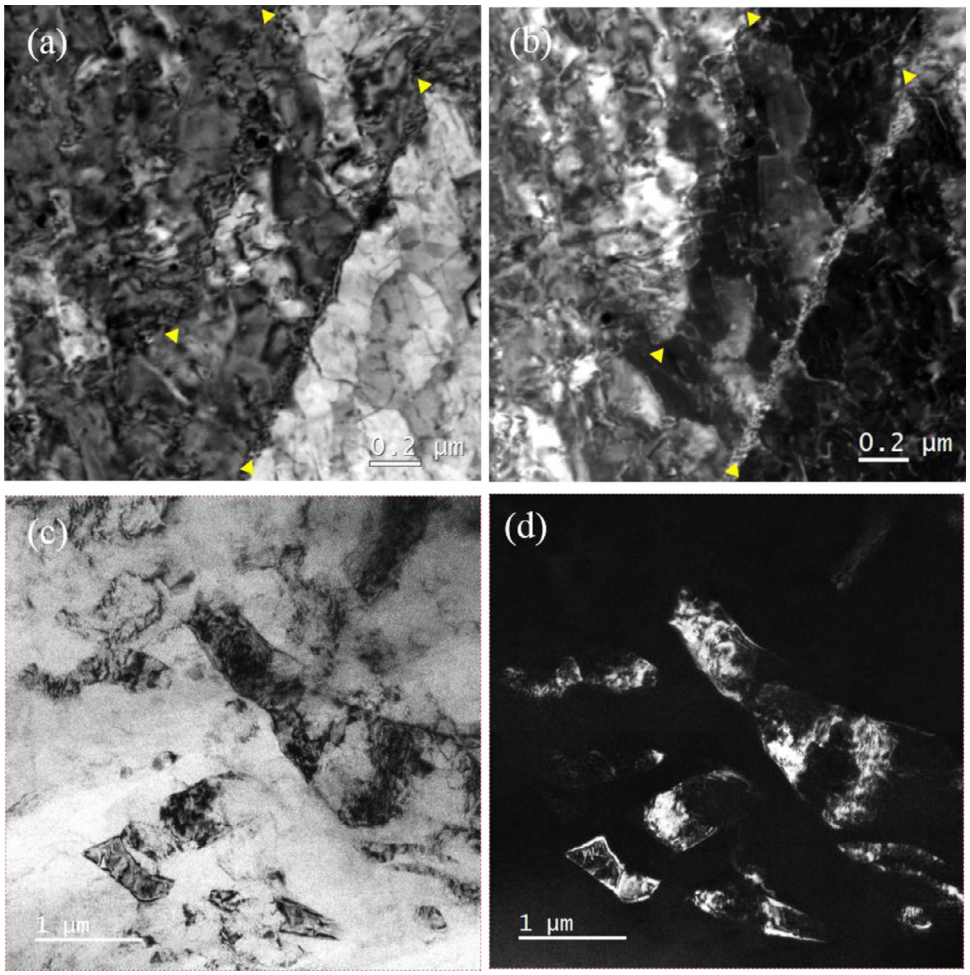

Fig. 5. Microstructure of sample M7 at 50 μm below the SSM-treated surface: (a) Bright field and (b) dark field TEM images showing lamellae bands with dislocations along and close to the lamellae boundaries. The yellow arrows mark the positions of the lamellae boundaries. (c) Bright field and (d) dark field images of polygonal micron to submicron sized grains.

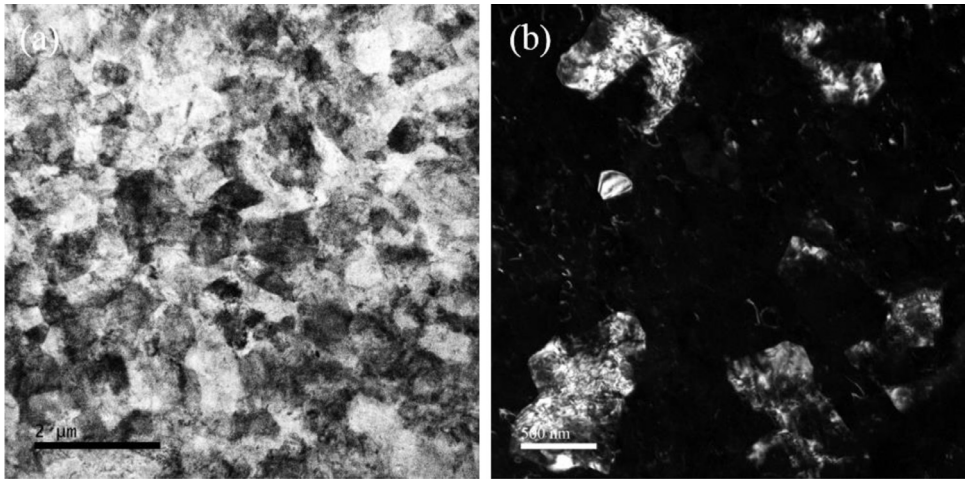

Fig. 6. (a) Bright field and (b) dark field TEM images showing ultrafine grained microstructure.

multi-directional and repetitive surface impacts can increase the possibility to form more than one twin variants in the Mg grains. Twin lamellae of the same twin variant may grow rapidly and combine with each other to form coarser twins. Propagation and growth of intersecting {10-12} twin variants will lead to the development of twin meshes. As the strain increases, for example, when larger milling balls or longer treatment time were used, twin-twin intersection and/or the relatively harder to form {10-11} contraction twins were observed by EBSD analysis (Fig. 11). A gradient twin mesh structure formed as a result of {10-12} tensile twin and possibly {10-11} contraction twin formation as the

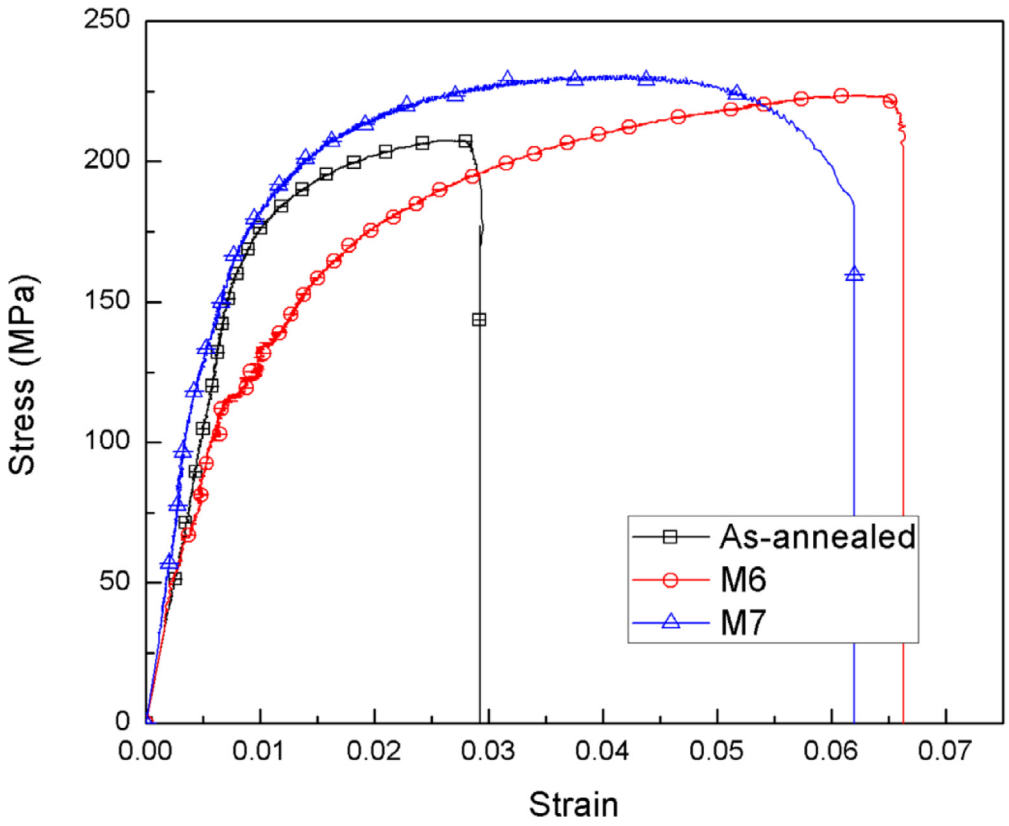

Fig. 7. Tensile mechanical behavior of the SSM treated Mg.

Table 3
Mechanical data for Mg with and without SSM treatment.

Sample	$\sigma_{0.2\%}$ (MPa)	UTS (MPa)	Strain at fracture (%)	Elongation (%)
As-annealed	178	207	2.9%	2.0%
M6	118	223	6.7%	5.5%
M7	171	230	6.2%	5.6%

strain increased. The twin meshes not only reduce the length scale of the rolled Mg microstructure, but also randomize its strong basal texture. {10-12} twins in Mg will reorient the matrix by ~86° about the ⟨11-20⟩ axis, and {10-11} twins will cause a ~56° grain reorientation about ⟨11-20⟩. Therefore, the formation of deformation twins can be associated with the randomized basal texture of the SSM-treated samples.

The nature of deformation twins in the SSM-treated sample was investigated in more detail using EBSD; correlated misorientation angle (i.e., misorientation angles calculated from neighboring grain or twin pairs) distributions for as-annealed Mg and SSM-treated Mg are shown in Fig. 11. In the distribution of misorientation angles for the as-annealed sample, there is a distinct intensity peak at ~30°, which is often observed in Mg and Mg alloys after thermomechanical processing at elevated temperatures. The fraction of misorientation angles around 86° is low in the as-annealed sample, indicating that the as-annealed Mg was nearly free of twins. In contrast, in the SSM-treated samples, peaks in intensity are observed at ~86° and ~60° in the grain boundary misorientation distribution profiles in Fig. 11 (b-j), corresponding to the formation of {10-12} extension twins with 86°<11-20> misorientation, and intervariants {10-12} twin-twin boundaries with 60°<1-100> misorientation or {10-11} contraction twins with 56°<11-20> misorientation, respectively. The distribution of rotation axes for misorientation-angle ranges of (86 ± 5)° and (60 ± 5)° in samples M1-M9 are plotted in the insets of Fig. 11. The ~86° rotation axes are predominantly centered around the ⟨11-20⟩ axes, which is consistent with the twin-matrix misorientation relationship for {10-12} twins. The majority of the rotation axes for ~60° misorientation are

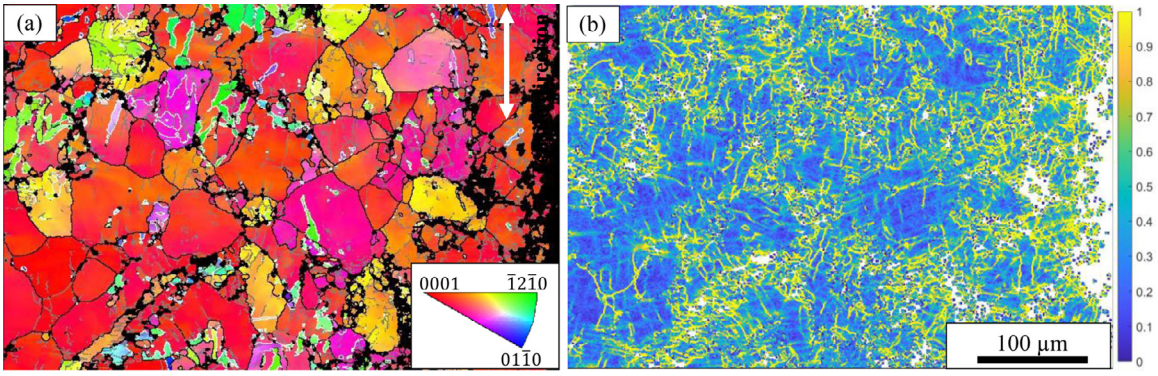

Fig. 8. EBSD analysis of sample M7 after tensile deformation: (a) inverse pole figure (IPF) colored map and (b) kernel average misorientation (KAM) map.

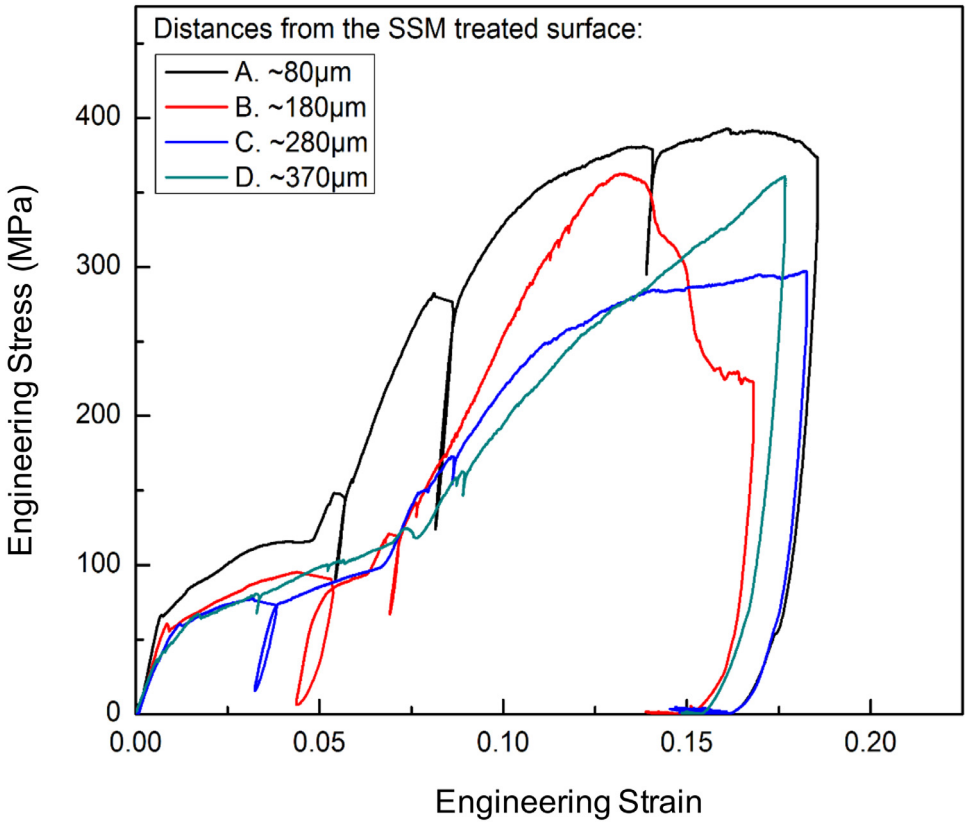

Fig. 9. Engineering stress-strain curves obtained from compression of micropillars fabricated at different distances from the SSM treated surface.

clustering around ⟨-1100⟩, corresponding to intervariants {10-12} twin-twin boundaries, and some are around ⟨11-20⟩, corresponding to {10-11} twin boundaries. We acknowledge that, limited by the resolution of SEM-based EBSD, fine twins may not be detected by this approach, and therefore our measured values represent a lower bound on the actual densities of twin boundaries and twin-twin boundaries.

The density profiles for different types of boundaries, including low angle grain boundaries (2°-10° misorientation angle), {10-12} twin boundaries ((86 ± 5)° misorientation angle) and intervariants twin-twin boundaries ((60 ± 5)° misorientation angle), are plotted in Fig. 12 for the as-annealed and SSM-treated samples. The densities were calculated from EBSD maps at three different depths, i.e., regions from 50 to 100 μm, 100 to 200 μm and 200 to 500 μm from the SSM-treated surface. In the as-annealed Mg sample, the densities of all types of strain induced defects are low. A gradient in microstructure is observed in all the SSM-treated samples, with generally higher amounts of low angle grain boundaries, twin and twin-twin boundaries at regions closer to the SSM-treated surfaces. The percentages of {10-12} twin boundaries and twin-twin boundaries increase from sample M1 to sample M2 to sample M3, as the diameter of milling balls increases from 0.1 mm to 0.9 mm. These results indicate that, with the same SSM treatment time of 2 min, when larger steel balls were used as milling media, higher densities of {10-12} extension twins were generated starting from the treated surface to the sample interior. The densities of low angle grain boundaries increase in the regions close to the treated surfaces, while in the sample interior, the densities are as low as that in the as-annealed sample. With a 2 mm milling ball size, when the SSM treatment time increases from 1 min to 2 min (sample M4 to sample M7), there is a saturation of twin boundary density and an increase in the density of low angle grain boundaries in regions away from the treated surfaces. The orientation of the treated surface also affects the SSM-treated microstructure, with slightly higher densities of twins being generated when the treated surfaces are parallel to the normal direction (see data for samples M4 and M6 versus samples M5 and M7, respectively). Finally, when the ball size and milling time are increased to 6.4 mm and 5 min, respectively, in M8, the density of twin boundaries starts to decrease and that for low angle grain boundaries continues to increase. The SSM parameters will be explored more systematically and robustly in future studies.

A high dislocation density in the matrix and within the twin domain are observed in TEM (Fig. 3). Twin boundaries and twin-twin intersections can pose obstacles to slip motion. Dislocation walls formed by planar rearrangement of dislocations were observed by TEM (Fig. 4 (b, c) and Fig. 5 (a, b)), which correspond to the low-angle grain boundaries observed ex-situ by EBSD (Fig. 4 (a). These low-angle sub-grain boundaries extended throughout the sample and caused the formation of the micron to submicron polygonal sub-grains being observed (Fig. 5). Finally, the formation of a uniformly distributed ultrafine grained structure was developed close to the SSM-treated surface, when the accumulated strain was sufficient (Fig. 8). A schematic description of the microstructural evolution with an increasing accumulation of strain during SSM is provided in Fig. 13.

4.2. Influence of SSM-induced microstructure on the deformation behavior

Tensile tests of Mg foils containing the SSM-treated surface layers exhibited an increase in tensile ductility and UTS when compared to the untreated as-annealed material (Fig. 7). From the tensile stress-strain curves, a longer uniform elongation region was observed in samples M6 and M7, characterized by a slower reduction in strain hardening rates compared to the as-annealed Mg. The misorientation profile for sample M7 after tensile deformation, generated from the EBSD data shown in Fig. 8a, is shown in Fig. 14. When compared to Fig. 11(h) for sample M7 before deformation, the positions of the intensity peaks remain similar. The peak in intensity at ~86° corresponds to {10-12} twin boundaries, and boundaries with 60°<1-

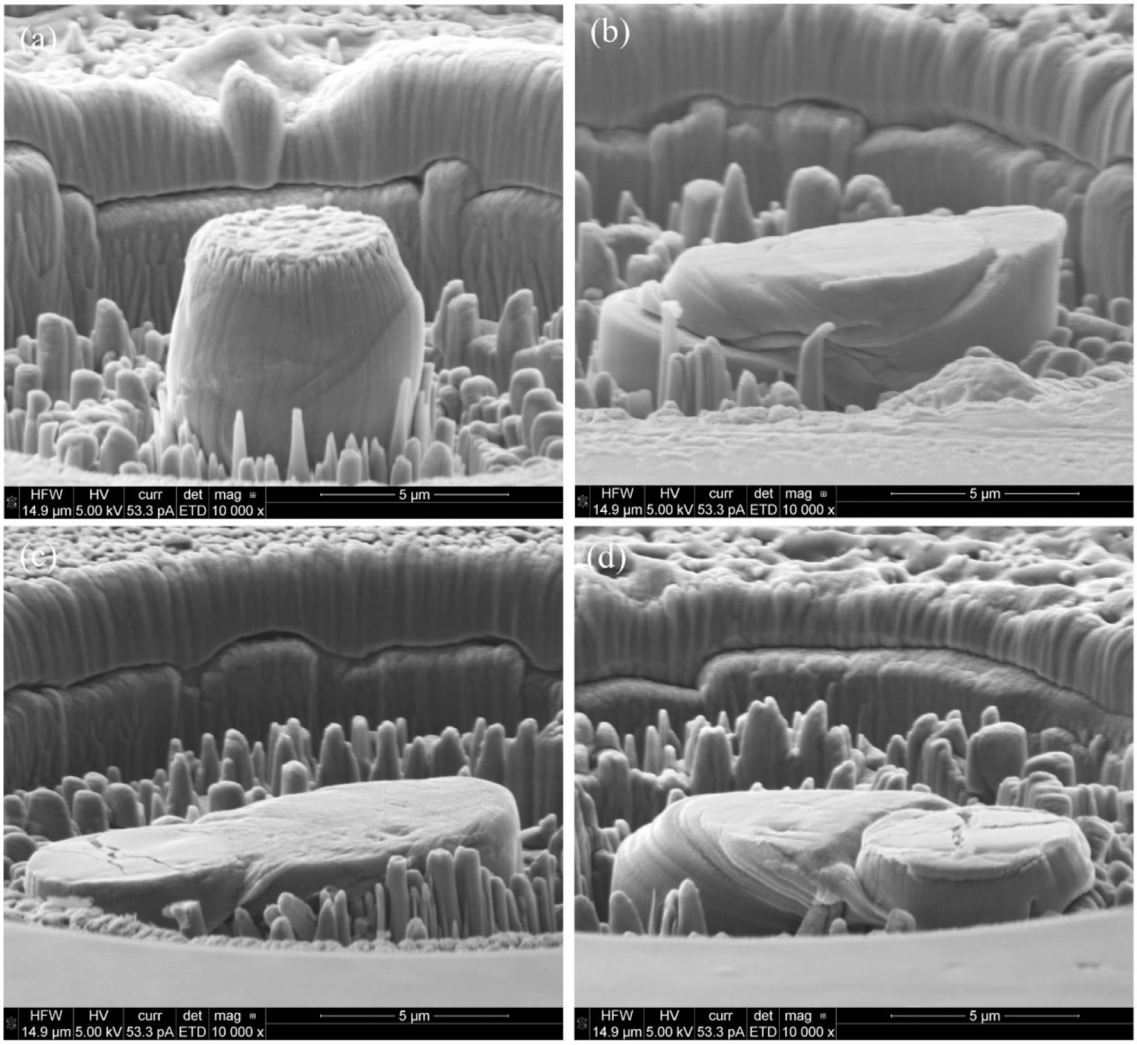

Fig. 10. SEM images of ~20% strain deformed micropillars at: (a) 80 μm, (b) 180 μm, (c) 280 μm and (d) 370 μm from the SSM treated surface.

100> misorientation are likely the intervariants {10-12} twin-twin boundaries. Since {10-12} twinning is not favored during tensile deformation in the rolling direction, i.e., tensile deformation perpendicular to the crystallographic c-axes, the twin boundaries and twin-twin boundaries are most likely generated by the SSM treatment and remain despite the tensile deformation. EBSD KAM analysis of the SSM-treated sample after tensile deformation (Fig. 8 (b)) indicates a high density of geometrically necessary dislocations at the SSM-treated surface layer due to the refined grain size. Intense strain accumulation was noted at the grain boundaries and, surprisingly, within grain interiors, e.g., close to the remaining twin boundaries. These observations suggest that twin boundaries form obstacles to dislocation slip, which may contribute to the strengthening of the SSM-treated Mg samples.

By combining the insight gained from the EBSD mapping and TEM observation, the mechanical response of the micropillars fabricated at various depths can be correlated with distinct microstructural features. Micropillar A at 80 μm beneath the SSM-treated surface is from the region where a high density of twin intersections is present, which leads to evident grain re-orientation and sub-division. Micropillar B at 180 μm originates from the region containing profuse twins with thicknesses ranging from hundreds of nanometers to several microns. Micropillars C and D, which span depths of 300 - 400 μm beneath the treated surface, exhibit a microstructure that is less deformed, as characterized by EBSD in Fig. 2 (h), and have a coarse-grain size and fewer twin boundaries. Observations from SEM *in-situ* compression confirm, first, that micropillar A exhibits an enhanced yield strength and strain hardening. Second, after ~19% compressive strain, micropillar A deformed without catastrophic failure compared to the micropillars further away from the SSM-treated surface. As seen from the stress-strain curves in Fig. 9, large stress drops occurred in the low-stress-plateau stage in micropillars B and C, corresponding to the fast propagation of a single shear band traversing the entire sample, as seen in supplementary videos S2 and S3, respectively. For micropillar A, no stress drop occurred before the end of the low-stress-plateau. Several non-catastrophic stress drops were observed at higher stress levels after the material starts to rapidly harden. Third, from the post-deformation SEM micrographs of the micropillars in Fig. 10, massive parallel slip bands, including that for the catastrophic major shear, were observed on the surface of micropillars C and D, while two or multiple orientations of slip traces were observed in micropillars B and A, respectively. For micropillar B, a shear band intersecting with the major catastrophic shear plane is clearly seen, indicating the activation of double slip modes. On the contrary, multiple minor shear displacements that did not cause sample failure can be seen in micropillar A. These findings suggest that the high density of twins and twin meshes close to the SSM-treated surface may be responsible for the activation of more slip systems and higher strain hardening in Mg that lead to material strengthening and toughening.

The mechanisms for such twin- and twin mesh- induced increases in strength observed in micropillar compression (Fig. 9) can be explained by slip-twin and twin-twin interactions, as supported by the post-deformation EBSD analysis (Fig. 8 and Fig. 14). In HCP metals,

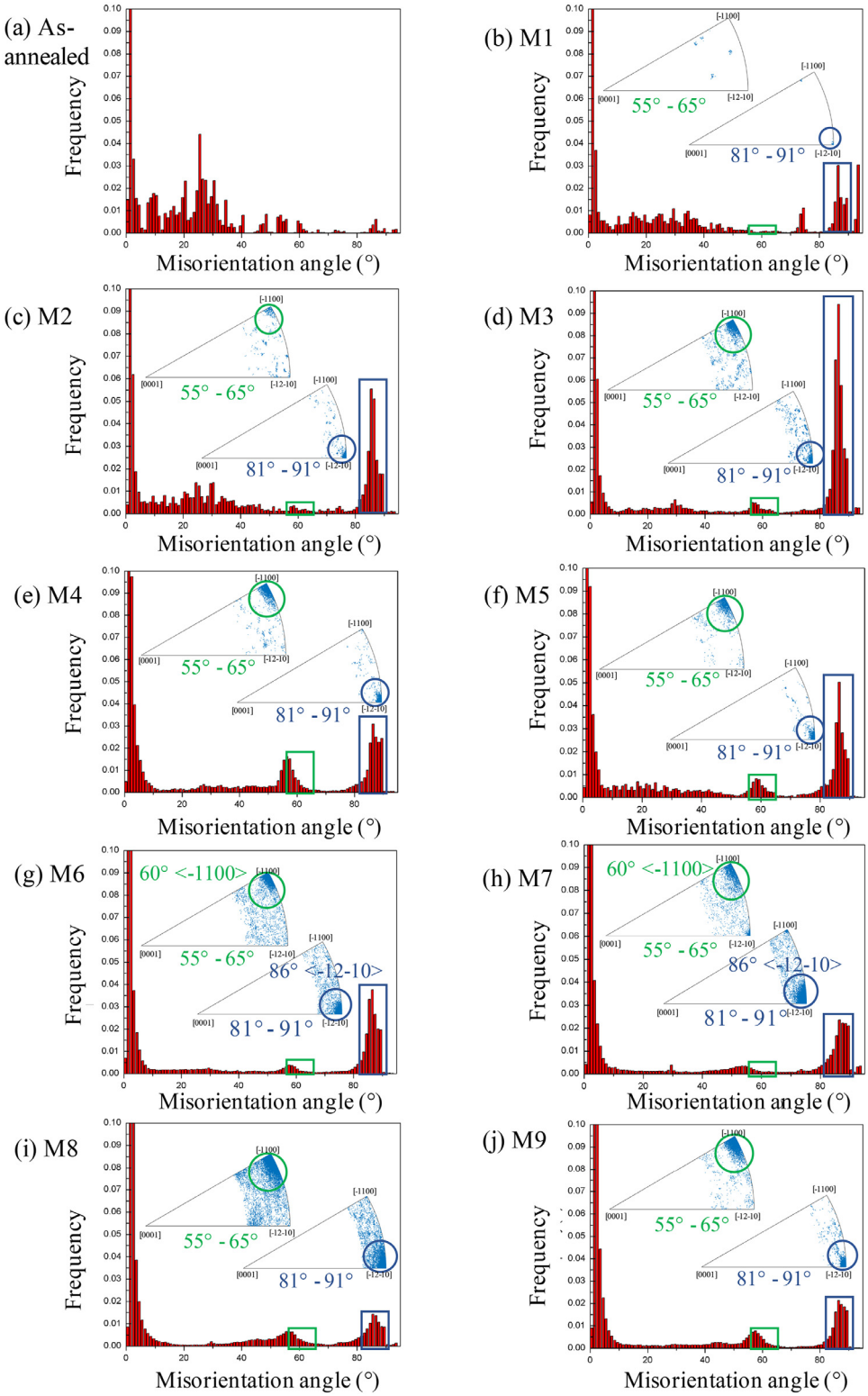

Fig. 11. Correlated misorientation profile of: (a) as-annealed Mg, (b) M1, (c) M2, (d) M3, (e) M4, (f) M5, (g) M6, (h) M7, (i) M8, (j) M9.

slip-twin interactions are known to lead to strengthening in HCP metals by three well-accepted mechanisms: 1) texture hardening due to lattice reorientation by twins, 2) the Basinski hardening mechanism due to transmutations of dislocations from glissile to sessile [44, 45], and 3) the obstacle effect of twin boundaries on dislocation slip [46]. The present TEM (Fig. 4) and post-deformation EBSD KAM analysis (Fig. 8 (b)) show evidence of the third contribution, in the form of dislocation accumulation developing at twin boundaries and twin-twin boundaries. This mechanism can also be seen from an absence of large shear steps and a higher strain hardening in micropillar A. Twin boundaries and twin-twin boundaries will act as strong barriers for slip to penetrate into the twinned regions, and incorporation or penetration into the twin boundaries can occur if necessary via dislocation reactions at these boundaries [6]. Many of these reactions are

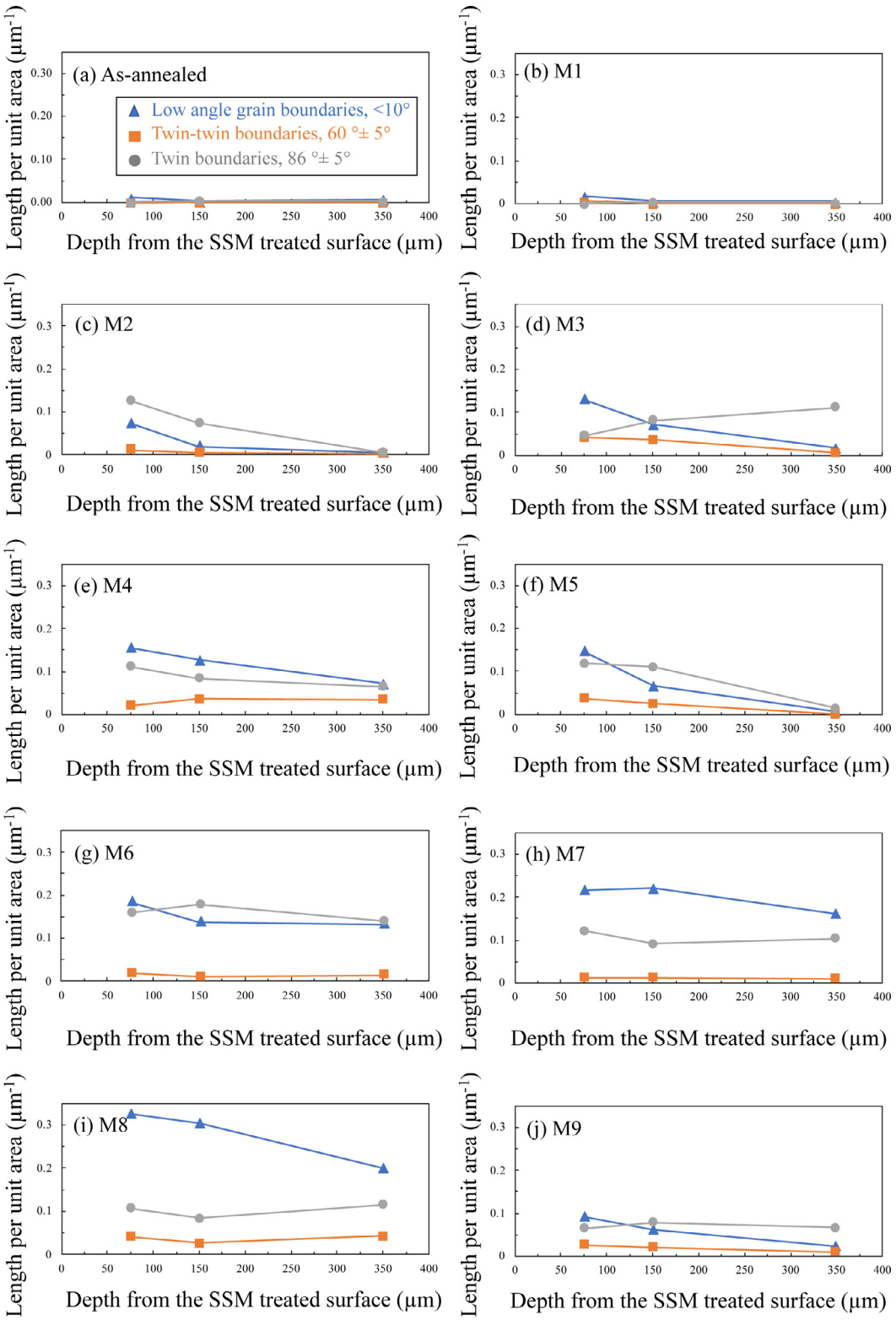

Fig. 12. Densities of low angle grain boundaries (LAGBs), {10-12} twin boundaries and twin-twin boundaries in the depth ranges of 50-100, 100-200 and 200-500 μm in (a) as-annealed Mg, (b) M1, (c) M2, (d) M3, (e) M4, (f) M5, (g) M6, (h) M7, (i) M8, (j) M9.

energetically unfavorable [6] and will take place only if there are sufficient stress concentrations arising at the head of dislocation pile-up. The introduction of twin boundaries therefore contributes to materials strengthening through a reduction in the dislocation mean free path. Moreover, the production of residual dislocations by these reactions could continue to serve as dislocation obstacles, which leads to an increase in strain hardening. Similarly, the twin-twin interactions being observed, like slip-twin interactions, can impede the further propagation and thickening of participating twins [15, 47]. As shown in the cases of body centered cubic metals, twin-twin intersections are

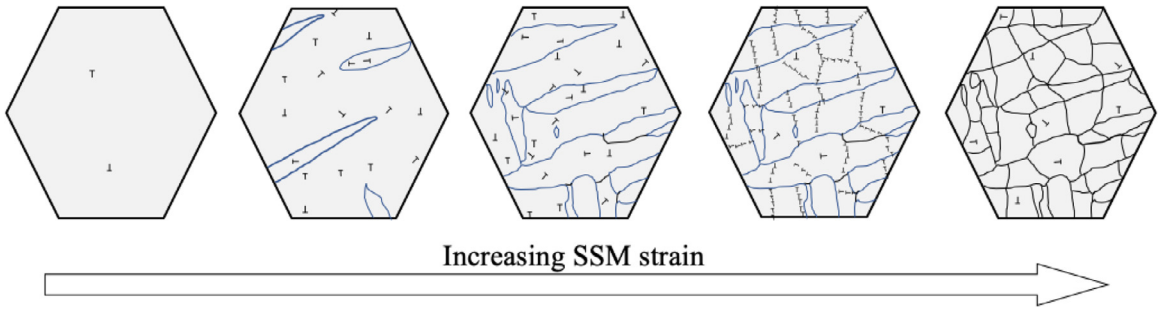

Fig. 13. Schematic of microstructural evolution during SSM. The boundaries in blue represent twin boundaries and the "T" symbols represent dislocations.

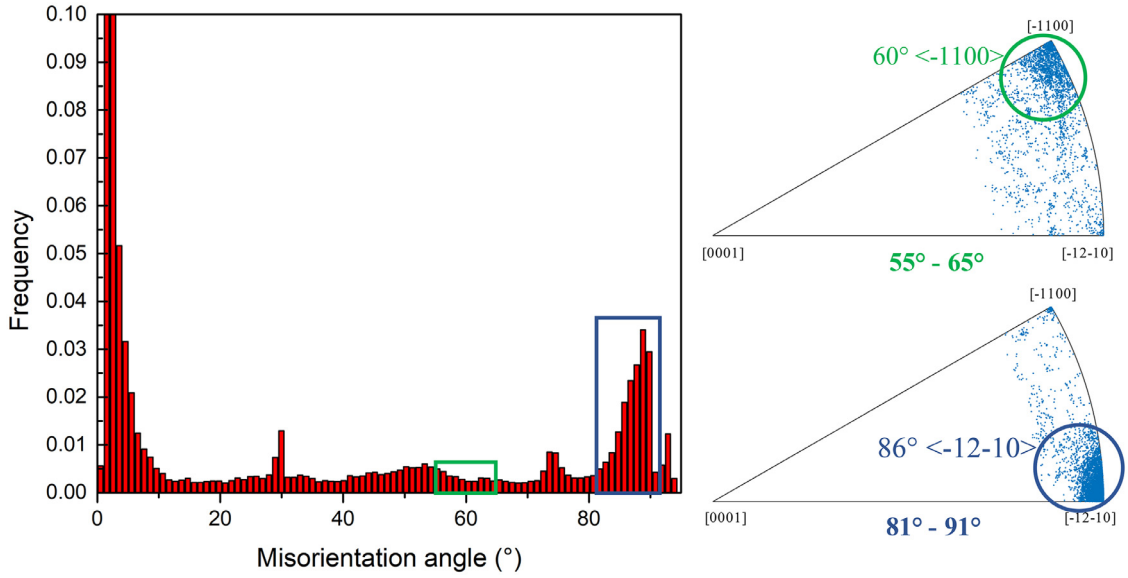

Fig. 14. Misorientation profile of sample M7 after tensile deformation and the corresponding distributions of rotation axes for misorientation-angle ranges of (86 ± 5)° and (60 ± 5)°.

accommodated by secondary twinning aided by stress relaxation by dislocation dissociations [16, 48]. These studies illustrate that the accommodation of strain can only be accomplished if the externally applied stress is locally enhanced by the presence of dislocation pile-up. Yu et. al. [40] suggested that back-stresses induced by the pile-up of boundary dislocations at twin-twin intersections may impede the motion of twinning dislocations, thus making further propagation and growth of twins more difficult. Taken together, it is envisaged that the presence of high densities of twin boundaries or twin-twin boundaries in SSM-treated Mg is likely to increase the rate of strain accumulation and consequently leads to a higher strain hardening rate.

Twinning can also enhance the ductility of Mg by increasing strain hardening and randomizing the texture. The twinning capabilities of activating dislocation slip and relaxing the slip system requirement can contribute to twin mesh induced plasticity. During tensile deformation in the rolling direction, most grains in the as-annealed rolled Mg foil are in the "hard-to-deform" orientations, and non-basal slip with high CRSS values need to be activated to accommodate the strain. Deformation twins can reorient the crystals to "softer" orientations, and deformation modes with low CRSS values, such as basal slip, in twins can further accommodate strain. This also explains the mild decrease in yield strength of the gradient twin mesh structure as a whole. Another explanation for the decrease in yield strength is the migration and detwinning of twin meshes. Further stabilization of the twin mesh structures may help increase the tensile yield strength of the SSM-treated samples.

5. Conclusions

In this work, we aim to create and investigate the effect of twin meshes on the tensile and compression response of polycrystalline pure Mg. A surface mechanical attrition strategy was used to impose repetitive, multi-directional loads on the sample surface using a SPEX milling treatment (SSM) to achieve a gradient microstructure consisting of a variation from an ultrafine grained to a twin-meshed structure, in a hot-rolled commercially-pure Mg sample. The main conclusions from the microstructural characterization and mechanical testing are as follows:

1. The SSM treatment was effective in creating gradient twin meshes, defined as two or more intersecting variants of {10-12} and {10-11} twins at the grain level. The character of the gradient structure varies, depending on the SSM parameters.
2. The twin meshes being produced effectively randomized the initially strong texture of the starting material.
3. Significantly, the tensile test results demonstrated that the samples after SSM treatment show two-fold increases in tensile ductility and ultimate strength over the as-annealed hot-rolled Mg.
4. SEM *in-situ* compression testing at various locations within the gradient structure provide evidence that the deformation and failure modes correspond to the changes in the presence of twin meshes, grain orientation and grain size.
5. With increasing strain and strain rate, microstructure evolution occurs in Mg by formation and interaction of deformation twins, dislocation slip and development of dislocation walls, and grain

refinement by division by multiply-crossed twin lamellae into fine to ultrafine polygonal subgrains.

Declaration of Competing Interests

The authors declare that they have no known competing financial interests or personal relationships that could have appeared to influence the work reported in this paper.

Acknowledgements

The authors acknowledge financial support from the National Science Foundation (NSF CMMI-1729829, NSF CMMI-1729887, and NSF CMMI-1723539). We also acknowledge funding from the ONR–Defense University Research Instrumentation Program under grant N00014-11-1-0788, which supported the purchase of the Bruker/Hysitron Picoindentor system. Ms. Ruilin Wang's and Mr. Lewis Lin's assistance with SSM treatment and sample polishing is greatly appreciated.

Supplementary materials

Supplementary material associated with this article can be found in the online version at doi:10.1016/j.actamat.2020.05.021.

References

[1] P.G. Partridge, The crystallography and deformation modes of hexagonal close-packed metals, Int. Mater. Rev. 12 (1) (1967) 169–194.
[2] M.H. Yoo, Slip, twinning and fracture in hexagonal close-packed metals, Metall. Mater. Trans. A 12 (3) (1981) 409–418.
[3] T.M. Pollock, Weight loss with magnesium alloys, Science 328 (5981) (2010) 986–987.
[4] J. Koike, T. Kobayashi, T. Mukai, H. Watanabe, M. Suzuki, K. Maruyama, K. Higashi, The activity of non-basal slip systems and dynamic recovery at room temperature in fine-grained AZ31B magnesium alloys, Acta Mater. 51 (7) (2003) 2055–2065.
[5] W.B. Hutchinson, M.R. Barnett, Effective values of critical resolved shear stress for slip in polycrystalline magnesium and other hcp metals, Scr. Mater. 63 (7) (2010) 737–740.
[6] J.W. Christian, S. Mahajan, Deformation twinning, Prog. Mater. Sci. 39 (1-2) (1995) 1–157.
[7] L. Lu, Y. Shen, X. Chen, L. Qian, K. Lu, Ultrahigh strength and high electrical conductivity in copper, Science 304 (5669) (2004) 422–426.
[8] Y.F. Shen, L. Lu, Q.H. Lu, Z.H. Jin, K. Lu, Tensile properties of copper with nano-scale twins, Scr. Mater. 52 (10) (2005) 989–994.
[9] Y.H. Zhao, J.F. Bingert, X.Z. Liao, B.Z. Cui, K. Han, A.V. Sergueeva, A.K. Mukherjee, R.Z. Valiev, T.G. Langdon, Y.T. Zhu, Simultaneously increasing the ductility and strength of ultra–fine–grained pure copper, Adv. Mater. 18 (22) (2006) 2949–2953.
[10] K. Lu, L. Lu, S. Suresh, Strengthening materials by engineering coherent internal boundaries at the nanoscale, Science 324 (5925) (2009) 349–352.
[11] H. Wang, Z. You, L. Lu, Kinematic and isotropic strain hardening in copper with highly aligned nanoscale twins, Mater. Res. Lett. 6 (6) (2018) 333–338.
[12] H.T. Wang, N.R. Tao, K. Lu, Strengthening an austenitic Fe–Mn steel using nano-twinned austenitic grains, Acta Mater. 60 (9) (2012) 4027–4040.
[13] H.T. Wang, N.R. Tao, K. Lu, Architectured surface layer with a gradient nano-twinned structure in a Fe–Mn austenitic steel, Scr. Mater. 68 (1) (2013) 22–27.
[14] Y. Wei, Y. Li, L. Zhu, Y. Liu, X. Lei, G. Wang, Y. Wu, Z. Mi, J. Liu, H. Wang, H. Gao, Evading the strength–ductility trade-off dilemma in steel through gradient hierarchical nanotwins, Nat. Commun. 5 (1) (2014) 3580.
[15] S. Vaidya, S. Mahajan, Accommodation and formation of {1121} twins in co single-crystals, Acta Metall. 28 (8) (1980) 1123–1131.
[16] S. Mahajan, G.Y. Chin, Twin-slip, twin-twin and slip-twin interactions in co-8 wt percent fe alloy single-crystals, Acta Metall. 21 (2) (1973) 173–179.
[17] C.M. Cepeda-Jiménez, J.M. Molina-Aldareguia, M.T. Pérez-Prado, Origin of the twinning to slip transition with grain size refinement, with decreasing strain rate and with increasing temperature in magnesium, Acta Mater. 88 (2015) 232–244.
[18] M.R. Barnett, Twinning and the ductility of magnesium alloys: Part II. "Contraction" twins, Mater. Sci. Eng. A 464 (1–2) (2007) 8–16.
[19] P. Cizek, M.R. Barnett, Characteristics of the contraction twins formed close to the fracture surface in Mg–3Al–1 Zn alloy deformed in tension, Scr. Mater. 59 (9) (2008) 959–962.
[20] M. Lentz, M. Risse, N. Schaefer, W. Reimers, I.J. Beyerlein, Strength and ductility with $\{10\bar{1}1\}-\{10\bar{1}2\}$ double twinning in a magnesium alloy, Nat. Commun. 7 (2016) 11068.
[21] Y. Xin, M. Wang, Z. Zeng, M. Nie, Q. Liu, Strengthening and toughening of magnesium alloy by {1 0 −1 2} extension twins, Scr. Mater. 66 (1) (2012) 25–28.
[22] Q. Yang, B. Jiang, B. Song, J. Zhang, F. Pan, Improving strength and formability of rolled AZ31 sheet by two-step twinning deformation, JOM (2019).
[23] J.F. Nie, Y.M. Zhu, J.Z. Liu, X.Y. Fang, Periodic segregation of solute atoms in fully coherent twin boundaries, Science 340 (6135) (2013) 957–960.
[24] J.F. Nie, Effects of precipitate shape and orientation on dispersion strengthening in magnesium alloys, Scr. Mater. 48 (8) (2003) 1009–1015.
[25] J.D. Robson, N. Stanford, M.R. Barnett, Effect of precipitate shape on slip and twinning in magnesium alloys, Acta Mater. 59 (5) (2011) 1945–1956.
[26] H. El Kadiri, J. Kapil, A.L. Oppedal, L.G. Hector Jr, S.R. Agnew, M. Cherkaoui, S.C. Vogel, The effect of twin–twin interactions on the nucleation and propagation of twinning in magnesium, Acta Mater. 61 (10) (2013) 3549–3563.
[27] X. Wu, P. Jiang, L. Chen, F. Yuan, Y.T. Zhu, Extraordinary strain hardening by gradient structure, PNAS 111 (20) (2014) 7197.
[28] J. Ding, Q. Li, J. Li, S. Xue, Z. Fan, H. Wang, X. Zhang, Mechanical behavior of structurally gradient nickel alloy, Acta Mater. 149 (2018) 57–67.
[29] Z. Yin, X. Yang, X. Ma, J. Moering, J. Yang, Y. Gong, Y. Zhu, X. Zhu, Strength and ductility of gradient structured copper obtained by surface mechanical attrition treatment, Mater. & Des. 105 (2016) 89–95.
[30] J. Moering, X. Ma, G. Chen, P. Miao, G. Li, G. Qian, S. Mathaudhu, Y. Zhu, The role of shear strain on texture and microstructural gradients in low carbon steel processed by Surface Mechanical Attrition Treatment, Scr. Mater. 108 (2015) 100–103.
[31] M. Yang, Y. Pan, F. Yuan, Y. Zhu, X. Wu, Back stress strengthening and strain hardening in gradient structure, Mater. Res. Lett. 4 (3) (2016) 145–151.
[32] X. Liu, F. Yuan, Y. Zhu, X. Wu, Extraordinary Bauschinger effect in gradient structured copper, Scr. Mater. 150 (2018) 57–60.
[33] K.Y. Zhu, A. Vassel, F. Brisset, K. Lu, J. Lu, Nanostructure formation mechanism of α-titanium using SMAT, Acta Mater. 52 (14) (2004) 4101–4110.
[34] X.Y. Shi, Y. Liu, D.J. Li, B. Chen, X.Q. Zeng, J. Lu, W.J. Ding, Microstructure evolution and mechanical properties of an Mg–Gd alloy subjected to surface mechanical attrition treatment, Mater. Sci. Eng. A 630 (2015) 146–154.
[35] X. Meng, M. Duan, L. Luo, D. Zhan, B. Jin, Y. Jin, X.-x. Rao, Y. Liu, J. Lu, The deformation behavior of AZ31 Mg alloy with surface mechanical attrition treatment, Mater. Sci. Eng. A 707 (2017) 636–646.
[36] L. Zhang, Y. Zou, H. Wang, L. Meng, J. Liu, Z. Zhang, Surface nanocrystallization of Mg-3 wt.% Li-6 wt.% Al alloy by surface mechanical attrition treatment, Mater. Charact. 120 (2016) 124–128.
[37] M.R. Barnett, Twinning and the ductility of magnesium alloys: Part I: "Tension" twins, Mater. Sci. Eng. A 464 (1–2) (2007) 1–7.
[38] S.R. Agnew, Ö. Duygulu, Plastic anisotropy and the role of non-basal slip in magnesium alloy AZ31B, Int. J. Plast. 21 (6) (2005) 1161–1193.
[39] S. Sandlöbes, S. Zaefferer, I. Schestakow, S. Yi, R. Gonzalez-Martinez, On the role of non-basal deformation mechanisms for the ductility of Mg and Mg–Y alloys, Acta Mater. 59 (2011) 429–439.
[40] D. Bufford, Y. Liu, J. Wang, H. Wang, X. Zhang, In situ nanoindentation study on plasticity and work hardening in aluminium with incoherent twin boundaries, Nat. Commun. (2014) 5.
[41] J.C. Tan, M.J. Tan, Dynamic continuous recrystallization characteristics in two stage deformation of Mg–3Al–1 Zn alloy sheet, Mater. Sci. Eng. A 339 (1) (2003) 124–132.
[42] N. Dixit, K.Y. Xie, K.J. Hemker, K.T. Ramesh, Microstructural evolution of pure magnesium under high strain rate loading, Acta Mater. 87 (2015) 56–67.
[43] A. Levinson, R.K. Mishra, R.D. Doherty, S.R. Kalidindi, Influence of deformation twinning on static annealing of AZ31 Mg alloy, Acta Mater. 61 (16) (2013) 5966–5978.
[44] H. El Kadiri, A.L. Oppedal, A crystal plasticity theory for latent hardening by glide twinning through dislocation transmutation and twin accommodation effects, J. Mech. Phys. Solids 58 (4) (2010) 613–624.
[45] F. Wang, S.R. Agnew, Dislocation transmutation by tension twinning in magnesium alloy AZ31, Int. J. Plast. 81 (2016) 63–86.
[46] I.J. Beyerlein, C.N. Tomé, A dislocation-based constitutive law for pure Zr including temperature effects, Int. J. Plast. 24 (5) (2008) 867–895.
[47] Q. Yu, J. Wang, Y. Jiang, R.J. McCabe, N. Li, C.N. Tomé, Twin–twin interactions in magnesium, Acta Mater. 77 (0) (2014) 28–42.
[48] S. Mahajan, G.Y. Chin, Interaction of twins with existing substructure and twins in cobalt-iron alloys, Acta Metall. 22 (9) (1974) 1113–1119.